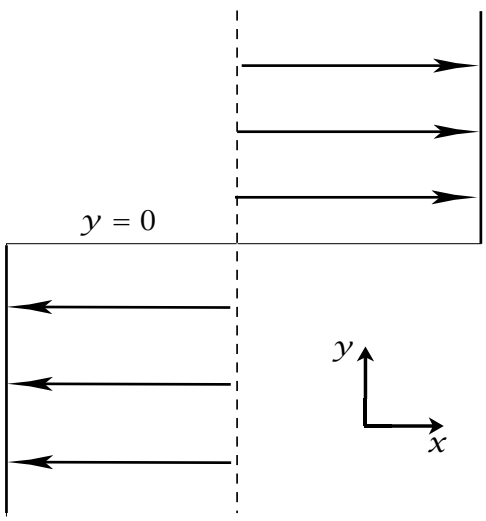

Fig. 6.1 A simple basic state giving rise to shear-flow instability. The velocity profile is discontinuous and the density is uniform.

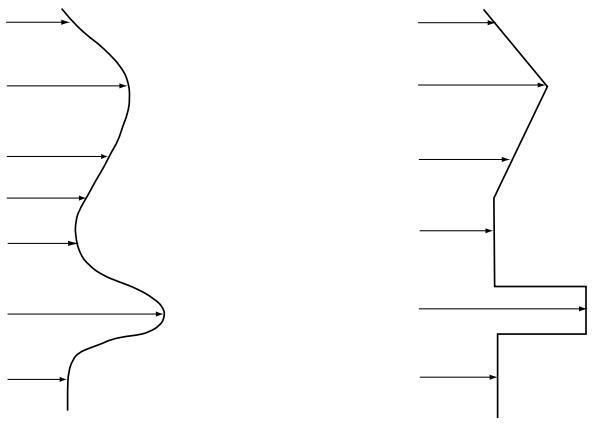

Fig. 6.2 Left: example of a smooth velocity profile — both the velocity and the vorticity are continuous. Right: example piecewise continuous profile — the velocity and vorticity may have finite discontinuities.

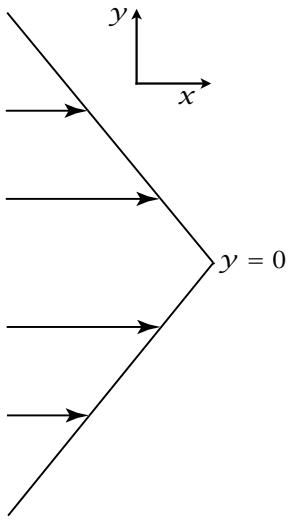

Fig. 6.3 Velocity profile of a point jet (so-called because the vorticity is concentrated at a point). Although the vorticity is discontinuous, a small perturbation gives rise only to *edge waves* centred at $y = 0$, and so the jet is stable.

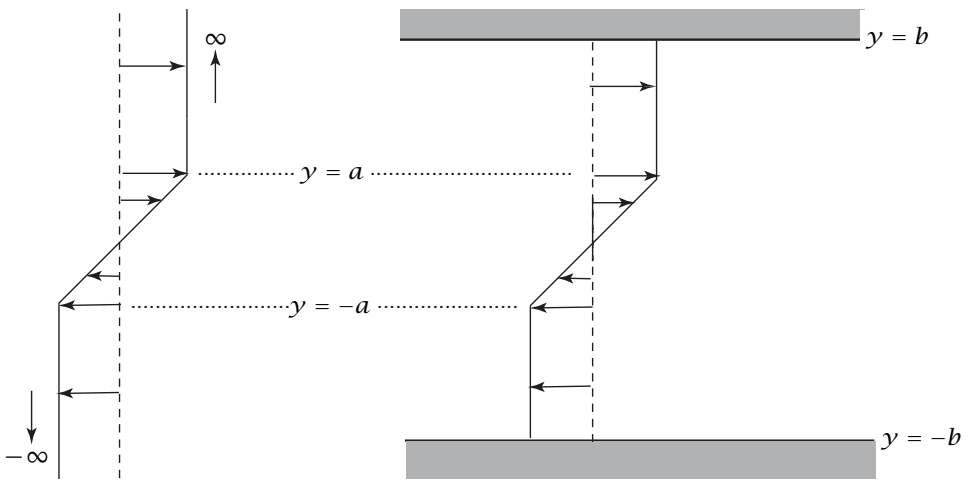

Fig. 6.4 Barotropically unstable velocity profiles. In the simplest case, on the left, a region of shear is sandwiched between two infinite regions of constant velocity. The edge waves at $y = \pm a$ interact to produce an instability. If $a = 0$, then the situation corresponds to that of Fig. 6.1, giving Kelvin–Helmholtz instability. In the case on the right, the flow is bounded at $y = \pm b$. It may be shown that the flow is still unstable, provided that b is sufficiently larger than a. If $b = a$ (plane Couette flow) the flow is stable to infinitesimal disturbances.

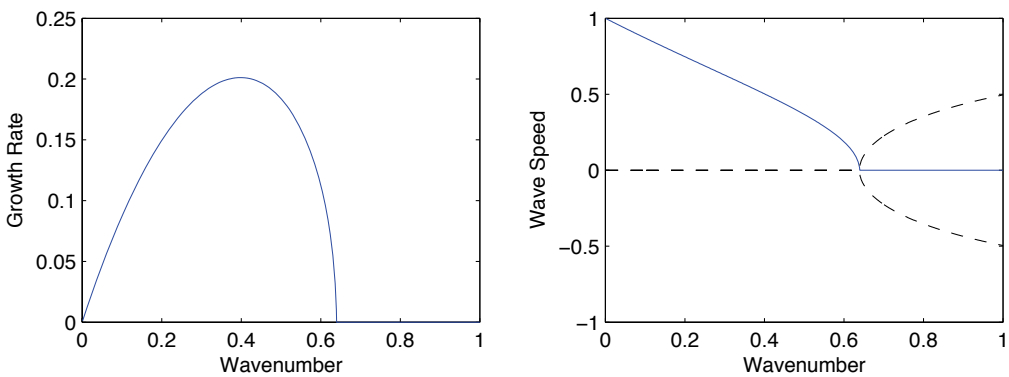

Fig. 6.5 Left: Growth rate ($\sigma = kc_i$) calculated from (6.42) with c non-dimensionalized by U_0 and k non-dimensionalized by $1/a$ (equivalent to setting $a = U_0 = 1$). Right: Real (c_r, dashed) and imaginary (c_i, solid) wave speeds. The flow is unstable for $k < 0.63$, with the maximum instability occurring at $k = 0.39$.

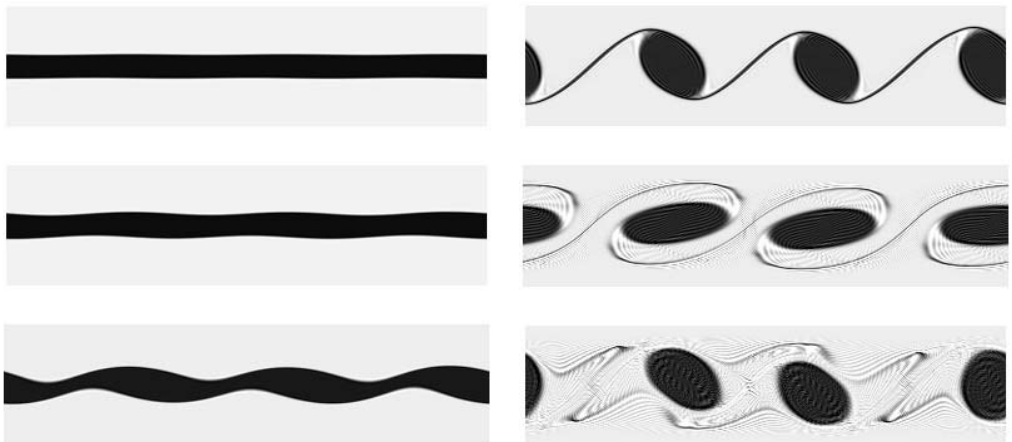

Fig. 6.6 A sequence of plots of the vorticity, at equal time intervals, from a numerical solution of the nonlinear vorticity equation (6.12), with initial conditions as in Fig. 6.4 with $a = 0.1$, plus a very small random perturbation. Time increases first down the left column and then down the right column. The solution is obtained in a rectangular (4×1) domain, with periodic conditions in the x-direction and slippery walls at $y = (0, 1)$. The maximum linear instability occurs for a wavelength of 1.57, which for a domain of length 4 corresponds to a wavenumber of 2.55. Since the periodic domain quantizes the allowable wavenumbers, the maximum instability is at wavenumber 3, and this is what emerges. Only in the first two or three frames is the linear approximation valid.

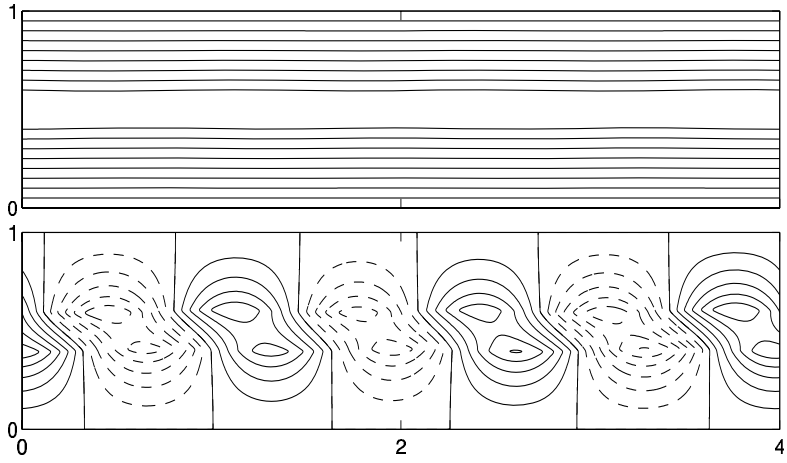

Fig. 6.7 The total streamfunction (top panel) and the perturbation streamfunction from the same numerical calculation as in Fig. 6.6, at a time corresponding to the second frame. Positive values are solid lines, and negative values are dashed. The perturbation pattern leans into the shear, and grows exponentially in place.

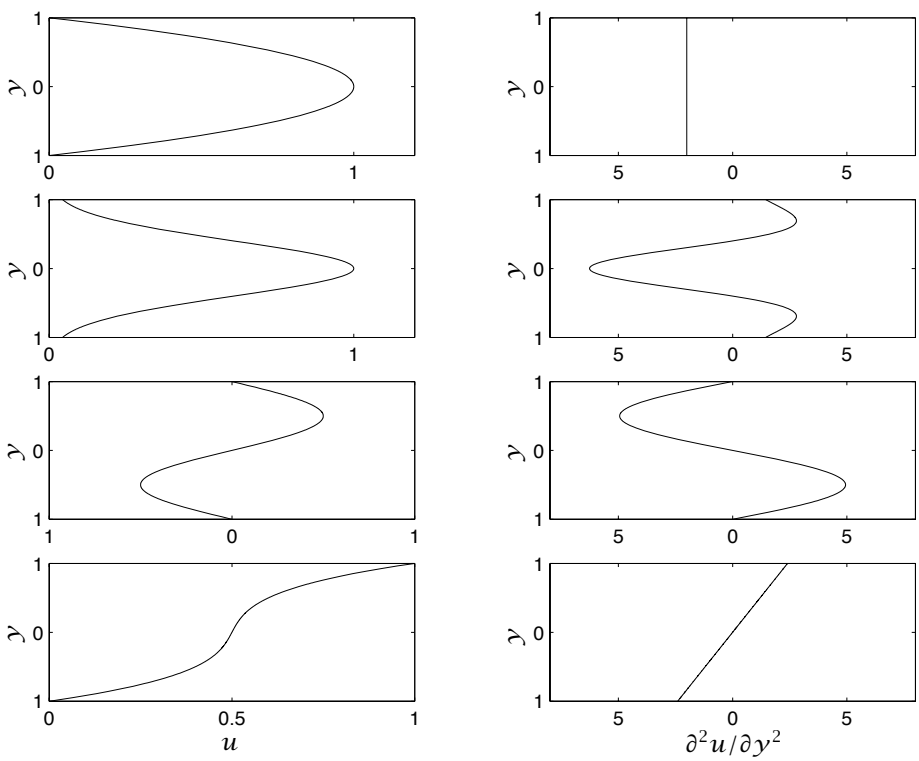

Fig. 6.8 Example parallel velocity profiles (left column) and their second derivatives (right column). From the top: Poiseuille flow ($u = 1 - y^2$); a Gaussian jet; a sinusoidal profile; a polynomial profile. By Rayleigh's criterion, the top profile is stable, whereas the lower three are potentially unstable. However, the bottom profile is stable by Fjørtoft's criterion (note that the vorticity maxima are at the boundaries). If the β-effect were present and large enough it would stabilize the middle two profiles.

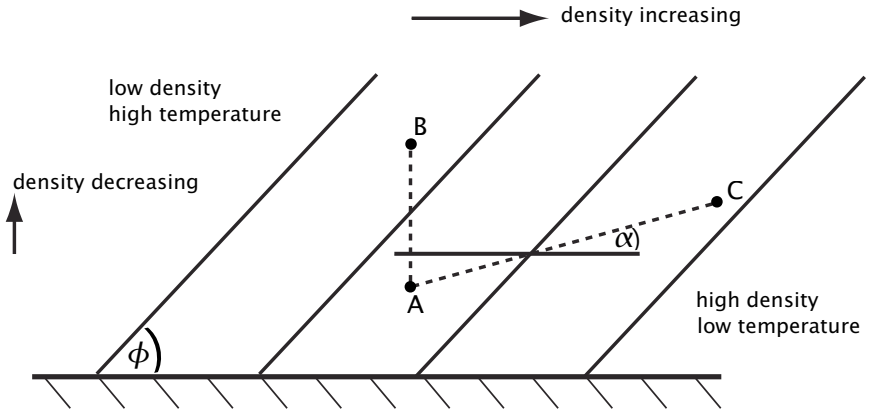

Fig. 6.9 A steady basic state giving rise to baroclinic instability. Potential density decreases upwards and equatorwards, and the associated horizontal pressure gradient is balanced by the Coriolis force. Parcel 'A' is heavier than 'C', and so statically stable, but it is lighter than 'B'. Hence, if 'A' and 'B' are interchanged there is a release of potential energy.

From Vallis (2006)

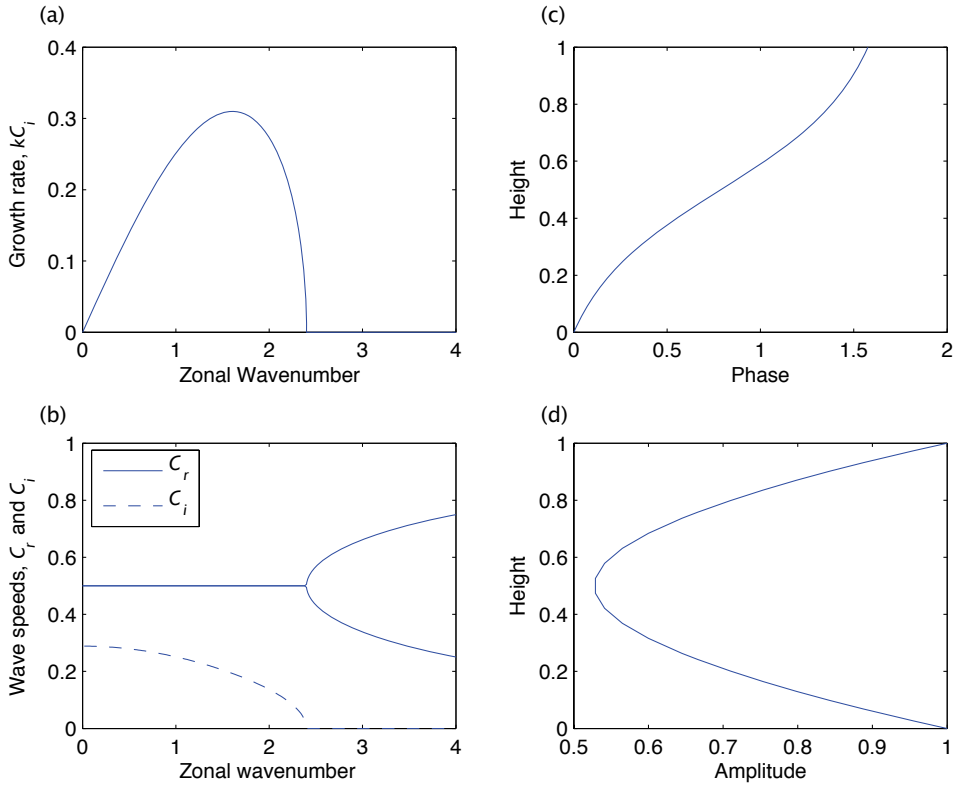

Fig. 6.10 Solution of the Eady problem, in non-dimensional units. (a) The growth rate, kc_i, of the most unstable Eady modes (i.e., those with the gravest meridional scale) as a function of scaled wavenumber μ, from (6.88) with $\Lambda = H = 1$. (b) The real (solid) and imaginary (dashed) wave speeds of those modes, as a function of horizontal wavenumber. (c) The phase of the single most unstable mode as a function of height. (d) The amplitude of that mode as a function of height. To obtain dimensional values, multiply the growth rate by $\Lambda H/L_d$ and the wavenumber by $1/L_d$.

From Vallis (2006)

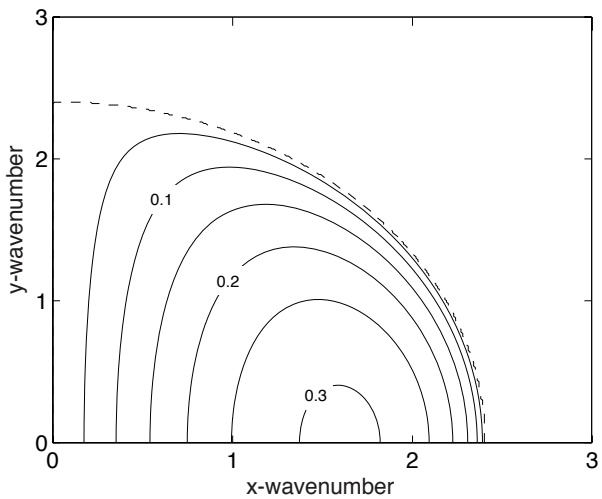

Fig. 6.11 Contours of the growth rate, σ, in the Eady problem, in the k–l plane using (6.88), non-dimensionalized as in Fig. 6.10. The growth rate peaks near the deformation scale, and for any given zonal wavenumber the most unstable wavenumber is that with the gravest meridional scale.

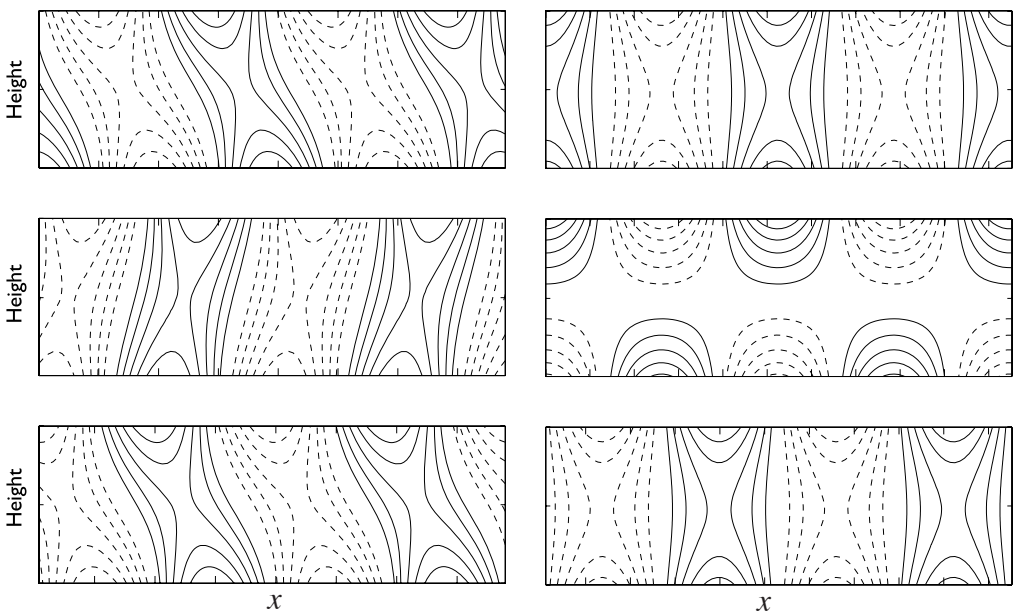

Fig. 6.12 Left column: vertical structure of the most unstable Eady mode. Top: contours of streamfunction. Middle: temperature, $\partial\psi/\partial z$. Bottom: meridional velocity, $\partial\psi/\partial x$. Negative contours are dashed, and two complete wavelengths are present in the horizontal direction. Poleward flowing (positive v) air is generally warmer than equatorward flowing air. Right column: the same, but now for a wave just beyond the short-wave cut-off.

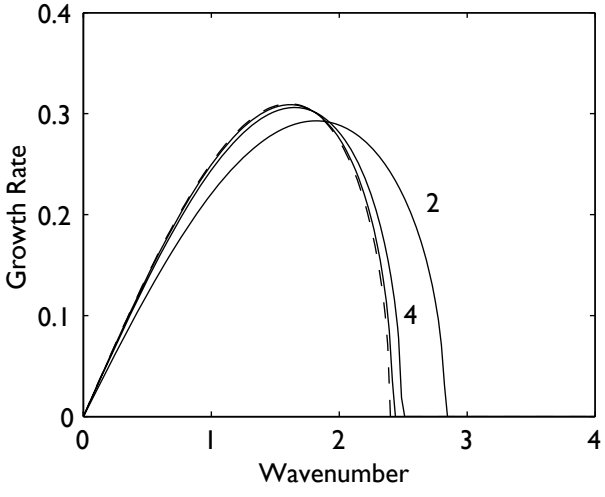

Fig. 6.13 Growth rates for models with varying numbers of vertical layers, all with $\beta = 0$ and the same uniform stratification and shear. The dashed line is the analytic solution to the continuous (Eady) problem, and the solid lines are results obtained using two, four and eight layers. The two- and four-layer results are labelled, and the eight-layer result is almost coincident with the dashed line.

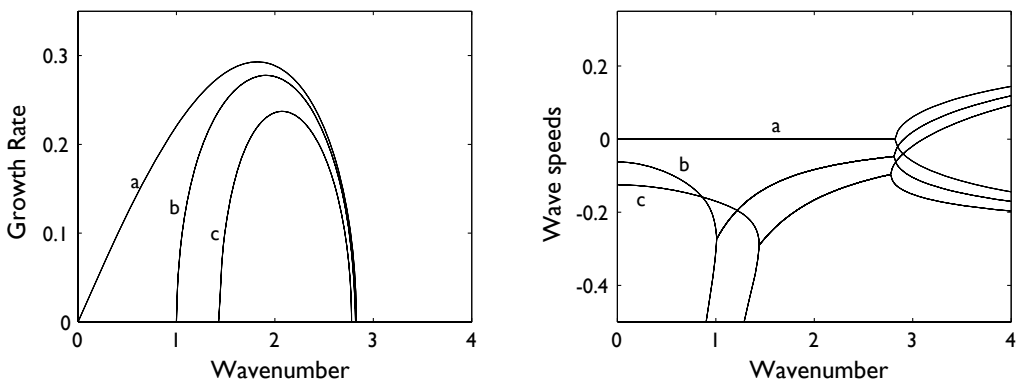

Fig. 6.14 Growth rates and wave speeds for the two-layer baroclinic instability problem, from (6.115), with three (non-dimensional) values of β: a, $\gamma = 0$ ($\hat{k}_\beta = 0$); b, $\gamma = 0.5$ ($\hat{k}_\beta = \sqrt{2}$); c, $\gamma = 1$ ($\hat{k}_\beta = 2$). As β increases, so does the low-wavenumber cut-off to instability, but the high-wavenumber cut-off is little changed. (The solutions are obtained from (6.115), with $\hat{k}_d = \sqrt{8}$ and $U_1 = -U_2 = 1/4$.)

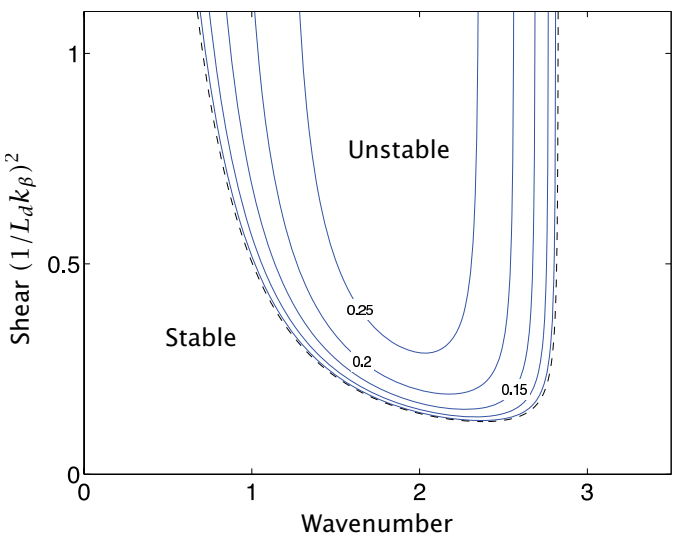

Fig. 6.15 Contours of growth rate in the two-layer baroclinic instability problem. The dashed line is the neutral stability curve obtained from (6.121), and the other curves are contours of growth rates obtained from (6.115). Outside of the dashed line, the flow is stable. The wavenumber is scaled by $1/L_d$ (i.e., by $k_d/\sqrt{8}$) and growth rates are scaled by the inverse of the Eady time scale (i.e., by U/L_d). Thus, for $L_d = 1000\,\text{km}$ and $U = 10\,\text{m}\,\text{s}^{-1}$, a non-dimensional growth rate of 0.25 corresponds to a dimensional growth rate of $0.25 \times 10^{-5}\,\text{s}^{-1} = 0.216\,\text{day}^{-1}$.

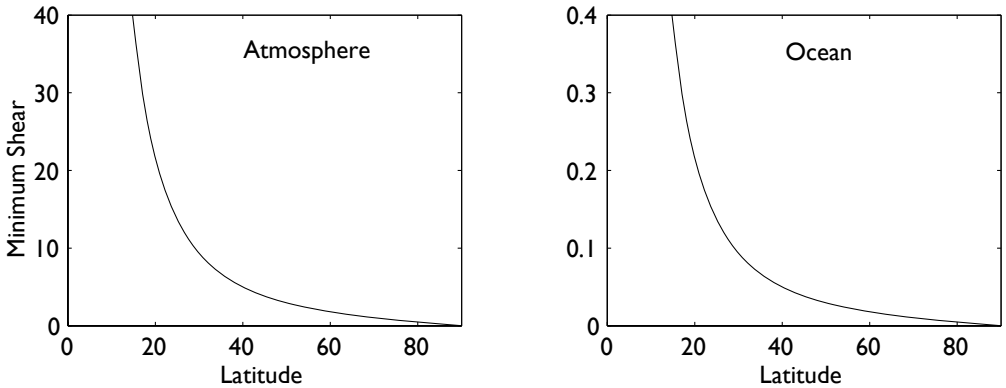

Fig. 6.16 The minimimum shear ($U_s = U_1 - U_2$, in $\mathrm{m\,s^{-1}}$) required for baroclinic instability in a two-layer model, calculated using (6.124), i.e., $U_s = \beta L_d^2/4$ where $\beta = 2\Omega a^{-1}\cos\vartheta$ and $L_d = NH/f$, with $f = 2\Omega\sin\vartheta$. The left panel uses $H = 10\,\mathrm{km}$ and $N = 10^{-2}\,\mathrm{s^{-1}}$, and the right panel uses parameters representative of the main thermocline, $H = 1\,\mathrm{km}$ and $N = 10^{-2}\,\mathrm{s^{-1}}$. The results are not quantitatively accurate, but the implications that the minimum shear is much less for the ocean, and that in both the atmosphere and the ocean the shear increases rapidly at low latitudes, are robust.

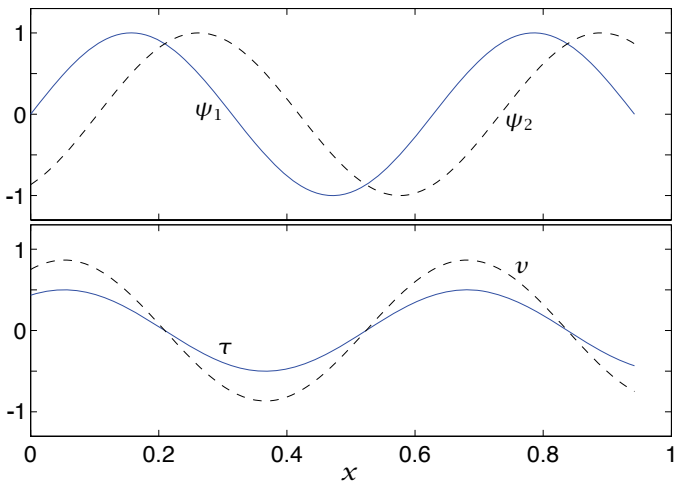

Fig. 6.17 Baroclinically unstable waves in a two layer model. The streamfunction is shown in the top panel, ψ_1 for the top layer and ψ_2 for the bottom layer. Given the westward tilt shown, the temperature, τ, and meridional velocity, v (bottom panel) are in phase, and the instability grows.

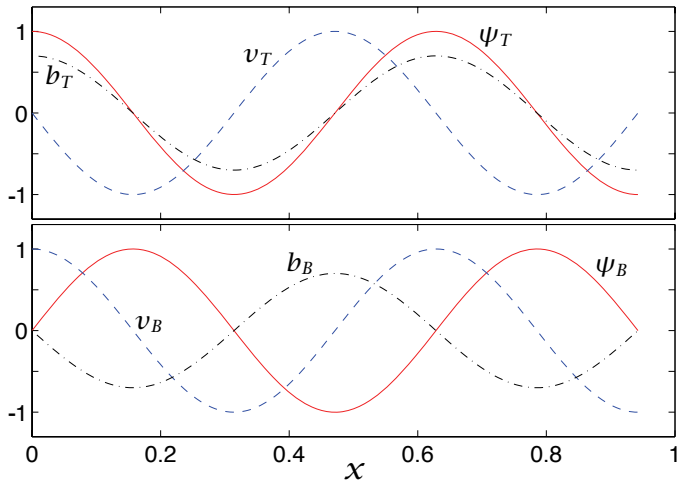

Fig. 6.18 Interacting edge waves in the Eady model. The upper panel shows waves on the top surface, and the lower panel show waves on the bottom. If the streamfunction tilts westward with height, then the temperature on the top (bottom) is correlated with the meridional velocity on the bottom (top), the waves can reinforce each other. See also Fig. 6.12.

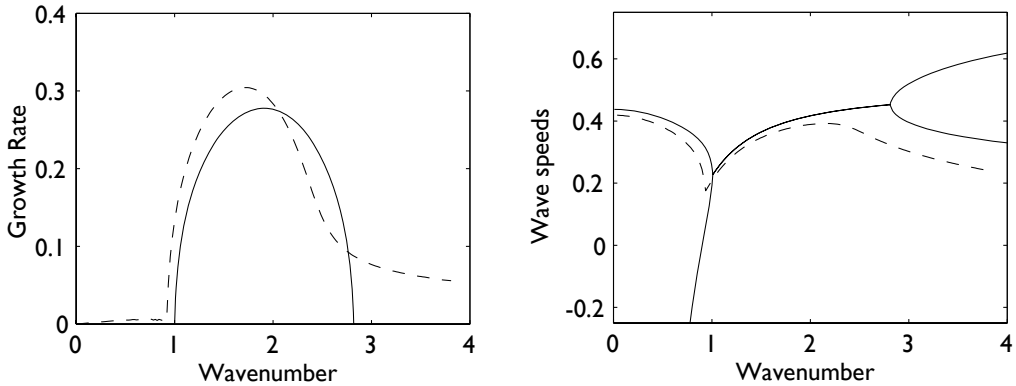

Fig. 6.19 Growth rates and wave speeds for the two-layer (solid) and continuous (dashed) models, with the same values of the Charney–Green number, γ, and uniform shear and stratification. (In the two-layer case $\gamma = \beta L_d^2/[2(U_1 - U_2)] = 0.5$, and in the continuous case $\gamma = \beta L_d^2/(H\Lambda) = 0.5$.) In the continuous case only the wave speed associated with the unstable mode is shown. In the two-layer case there are two real wave speeds which coalesce in the unstable region.

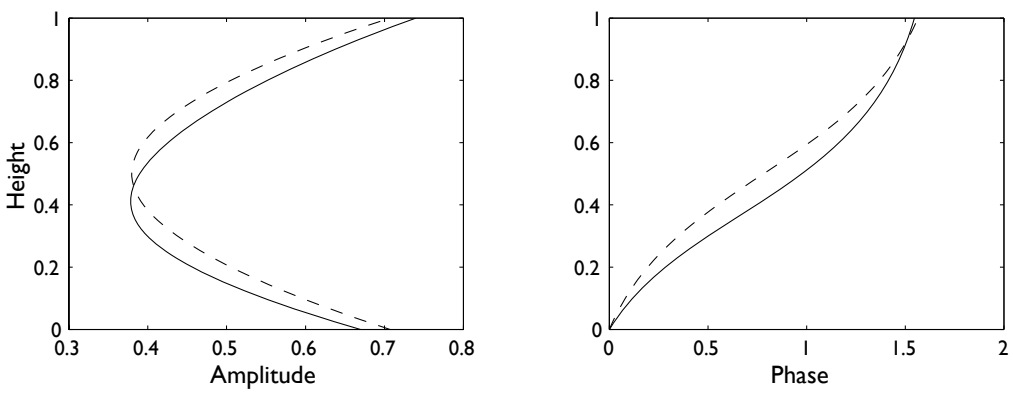

Fig. 6.20 Vertical structure of the most unstable modes in a continuously stratified instability calculation with $\beta = 0$ (dashed lines, the Eady problem) and $\beta \neq 0$ (solid lines), as in Fig. 6.19. The effect of beta is to depress the height of the maximum amplitude of the instability.

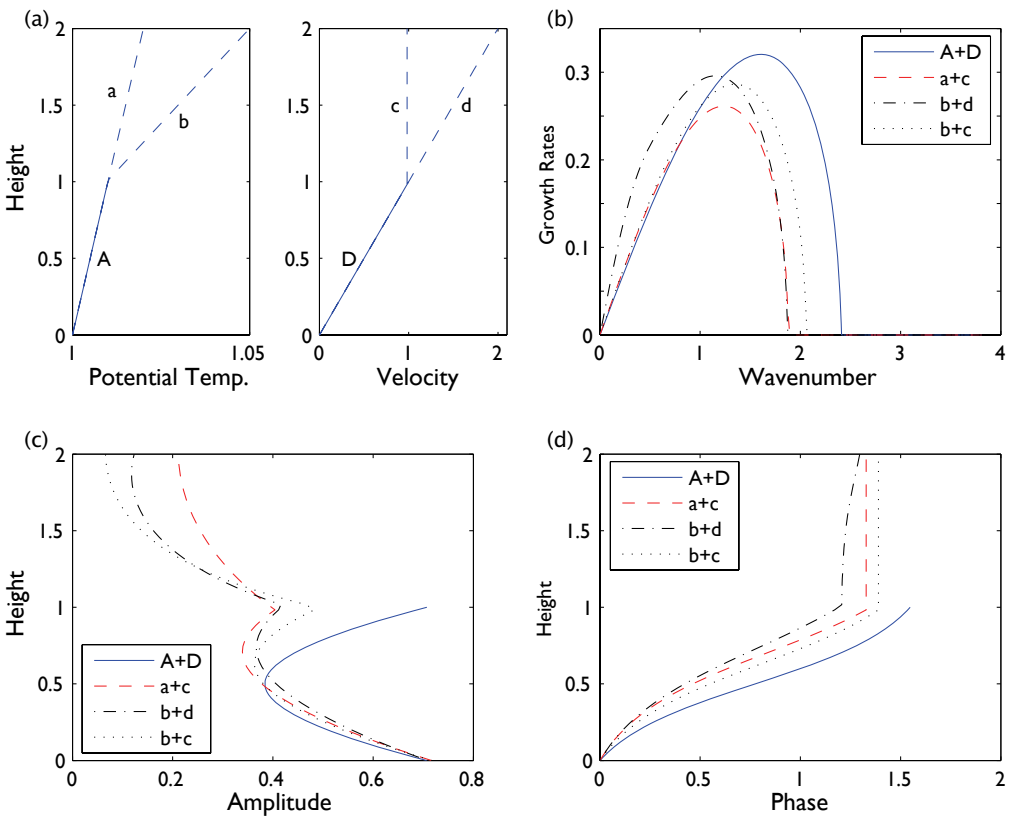

Fig. 6.21 The effect of a stratosphere on baroclinic instability: (a) the given profiles of shear and stratification; (b) the growth rate of the instabilities; (c) the amplitude of the most unstable mode as a function of height; (d) the phase of the most unstable mode. The instability problem is solved numerically with various profiles of stratification and shear. In each profile, in the idealized troposphere ($z < 1$) the shear and stratification are uniform and the same in each case. We consider four idealized stratospheres ($z \geq 1$): 1, A lid at $z = 1$, i.e., no stratosphere, giving the Eady problem itself (profiles A+D, solid lines); 2, stratospheric stratification as for the troposphere, but with zero shear (profiles a+c, dashed); 3, stratospheric shear as for troposphere, but with stratification (N^2) four times the tropospheric value (b+d, dot-dashed); 4, zero shear and high stratification in the stratosphere (b+c, dotted). In the troposphere the amplitude and structure of the instability are similar in all cases, illustrating the similarity of a rigid lid and abrupt changes in shear or stratification. Either a high stratification or a low shear (or both) will result in weak stratospheric instability.

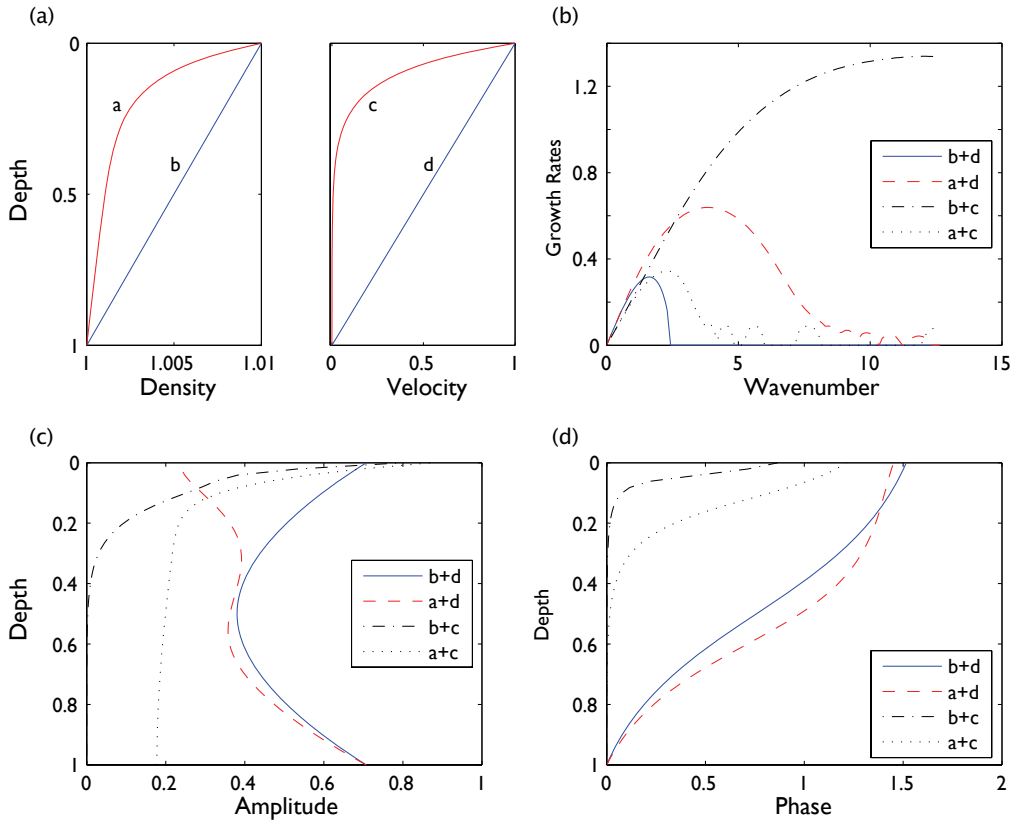

Fig. 6.22 The baroclinic instability in an idealized ocean, with four different profiles of shear or stratification. The panels are: (a) the profiles of velocity and density (and so N^2) used; (b) the growth rates of the various cases; (c) the vertical structure of the amplitude of the most unstable models; (d) the phase in the vertical of the most unstable modes. The instability is calculated numerically with four combinations of shear and stratification: 1, uniform stratification and shear i.e., the Eady problem, (profiles b+d, solid lines); 2, uniform shear, upper-ocean enhanced stratification (a+d, dashed); 3, uniform stratification, upper ocean enhanced shear (b+c, dot-dashed); 4, both stratification and shear enhanced in the upper ocean (a+c, dotted). Case 2 (a+d, dashed) is really more like an atmosphere with a stratosphere (see Fig. 6.21), and the amplitude of the disturbance falls off, rather unrealistically, in the upper ocean. Case 4 (a+c, dotted) is the most oceanically relevant.

From Vallis (2006)

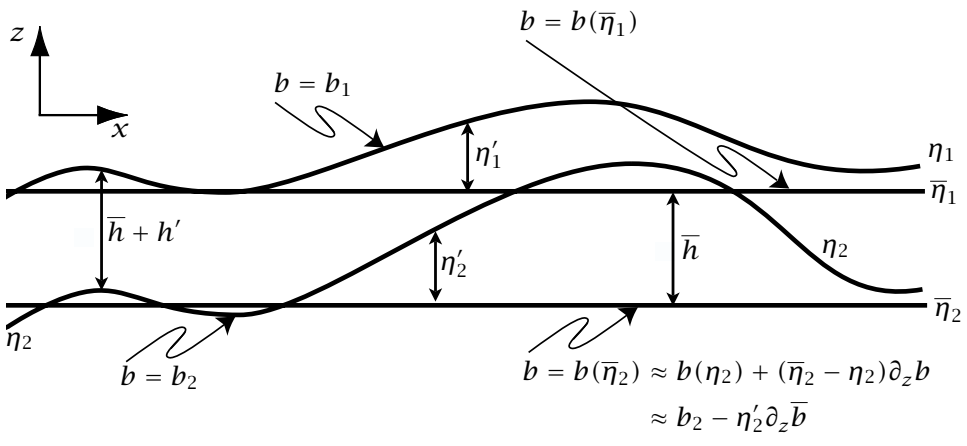

Fig. 7.1 Two isentropic surfaces, η_1 and η_2, and their mean positions, $\overline{\eta}_1$ and $\overline{\eta}_2$. The departure of an isentrope from its mean position is proportional to the temperature perturbation at the mean position of the isentrope, and the variations in thickness (h') of the isentropic layer are proportional to the vertical derivative of this.

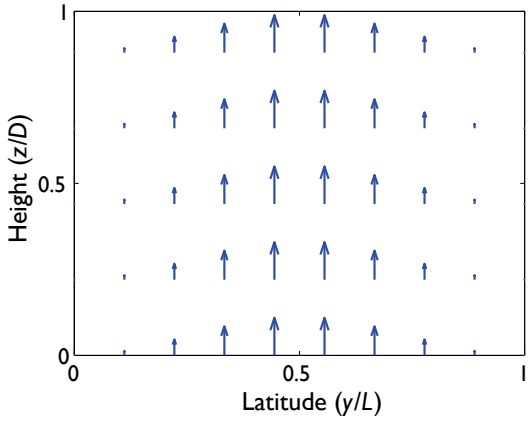

Fig. 7.2 The Eliassen–Palm vector in the Eady problem.

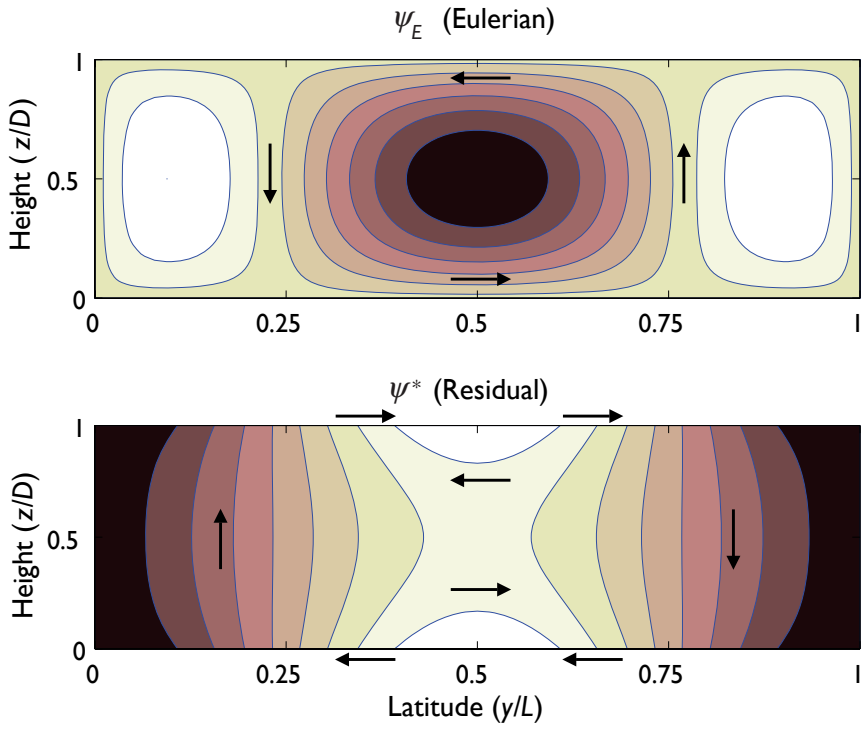

Fig. 7.3 The Eulerian streamfunction (top) and the residual streamfunction for the Eady problem, calculated using (7.135) and (7.136), with $L^2/L_d^2 = 9$.

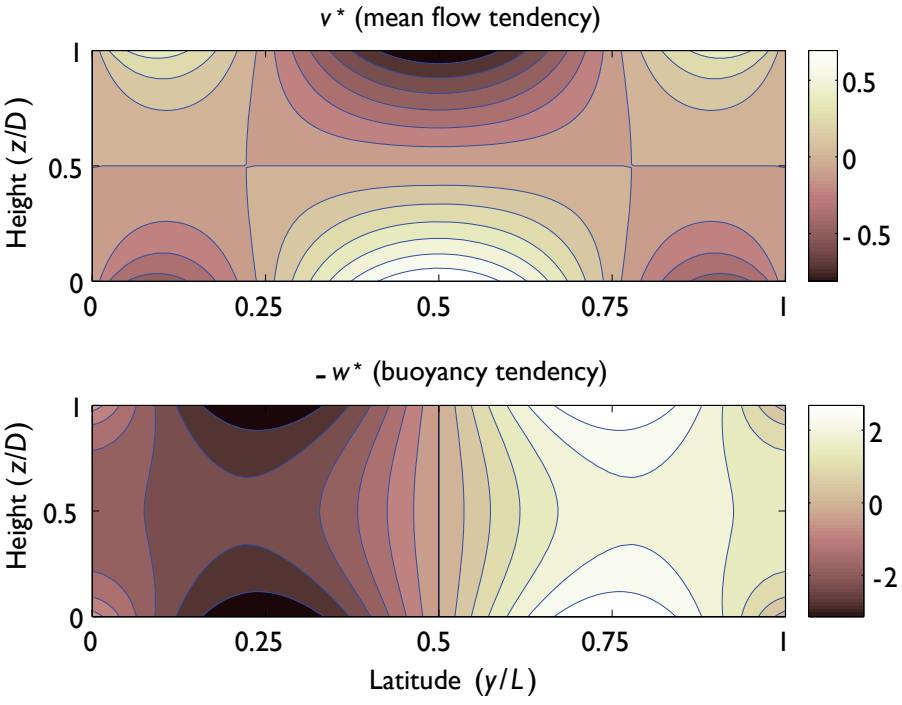

Fig. 7.4 The tendency of the zonal mean flow ($\partial\overline{u}/\partial t$) and the buoyancy ($\partial\overline{b}/\partial t$) for the Eady problem. Lighter (darker) shading means a positive (negative) tendency, but the units themselves are arbitrary.

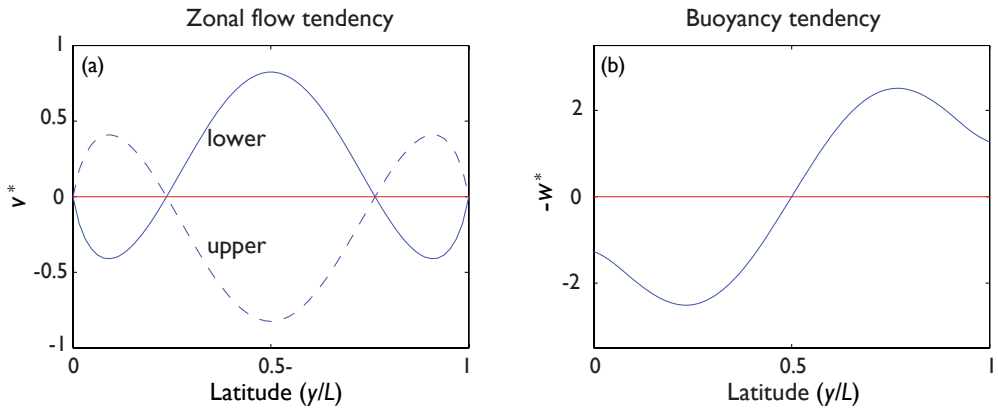

Fig. 7.5 (a) The tendency of the zonal mean flow ($\partial \overline{u}/\partial t$) just below the upper lid (dashed) and just above the surface (solid) in the Eady problem. The vertically integrated tendency is zero. (b) The vertically averaged buoyancy tendency.

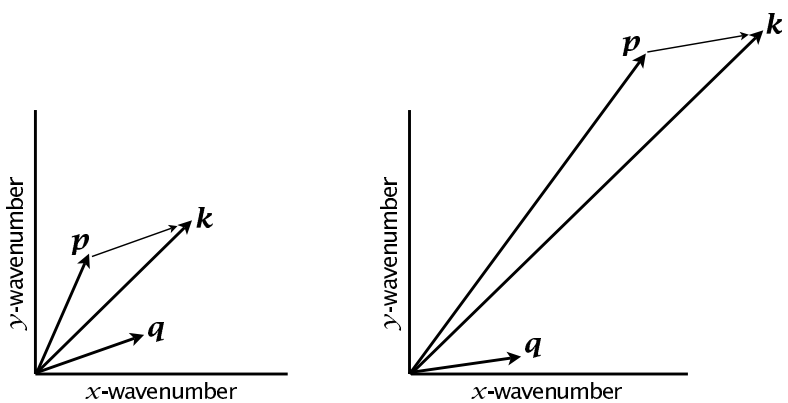

Fig. 8.1 Two interacting triads, each with $\boldsymbol{k} = \boldsymbol{p} + \boldsymbol{q}$. On the left, a local triad with $k \sim p \sim q$. On the right, a non-local triad with $k \sim p \gg q$.

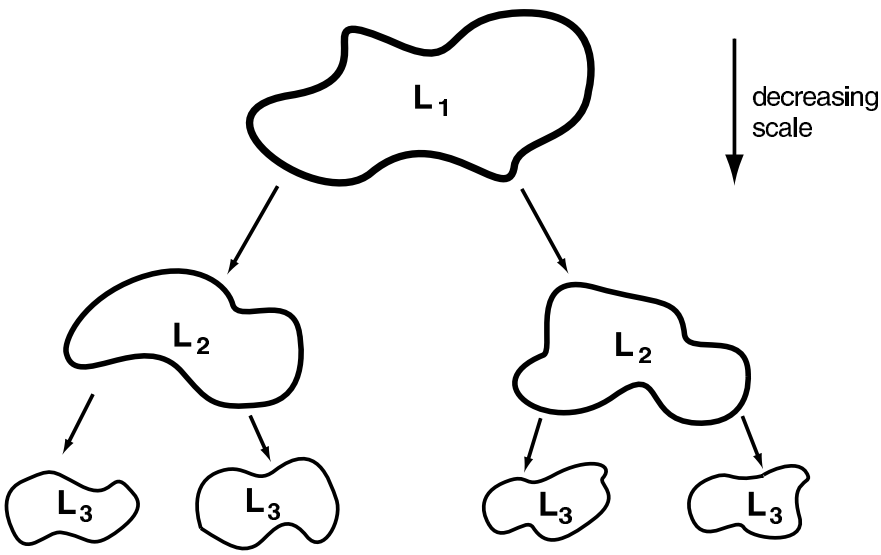

Fig. 8.2 Schema of the passage of energy to smaller scales: eddies at a large scale break up into smaller scale eddies, thereby transferring energy to smaller scales. If the passage occurs between eddies of similar sizes (i.e., if it is spectrally local) the transfer is said to be a cascade. The eddies in reality are embedded within each other.

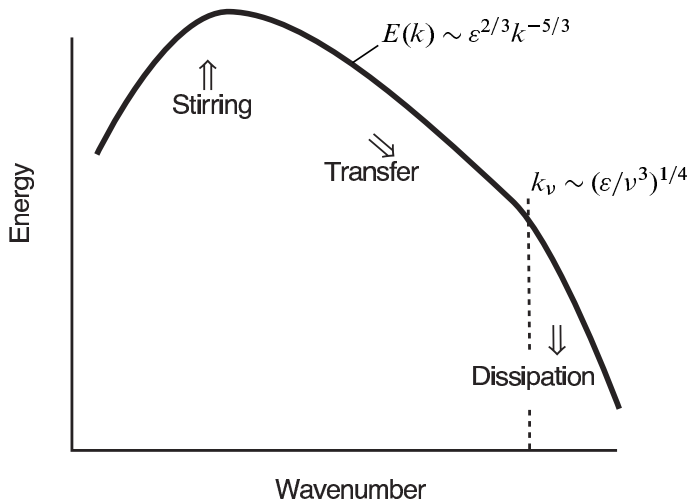

Fig. 8.3 Schema of energy spectrum in three-dimensional turbulence, in the theory of Kolmogorov. Energy is supplied at some rate ε; it is cascaded to small scales, where it is ultimately dissipated by viscosity. There is no systematic energy transfer to scales larger than the forcing scale, so here the energy falls off.

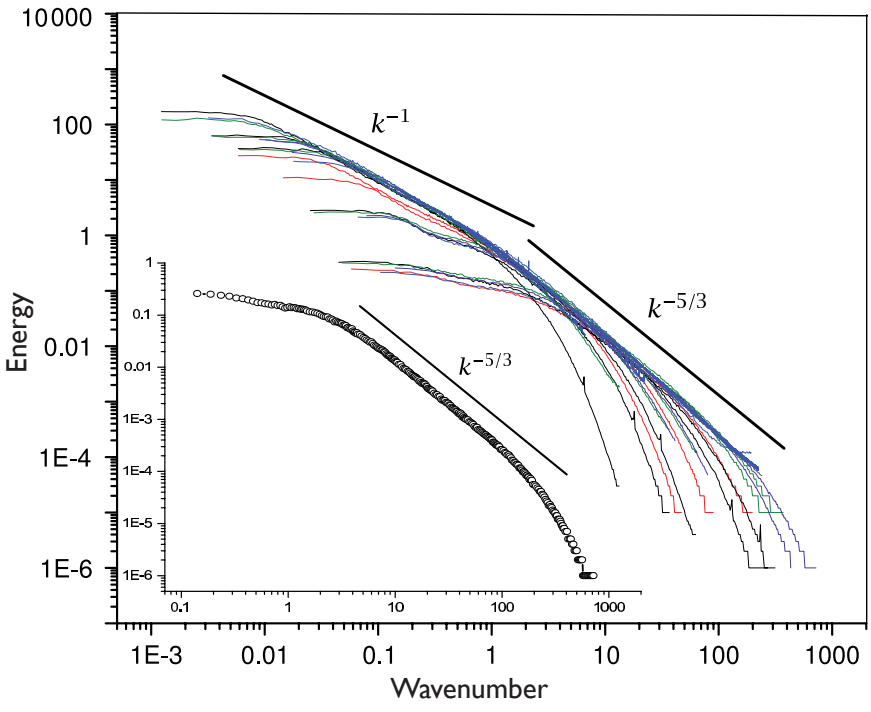

Fig. 8.4 The energy spectrum of 3D turbulence measured in some experiments at the Princeton Superpipe facility.[1] The outer plot shows the spectra from a large number of experiments at different Reynolds numbers up to 10^6, with the magnitude of their spectra appropriately rescaled. Smaller scales show a good $-5/3$ spectrum, whereas at larger scales the eddies feel the effects of the pipe wall and the spectra are a little shallower. The inner plot shows the spectrum in the centre of the pipe in a single experiment at $Re \approx 10^6$.

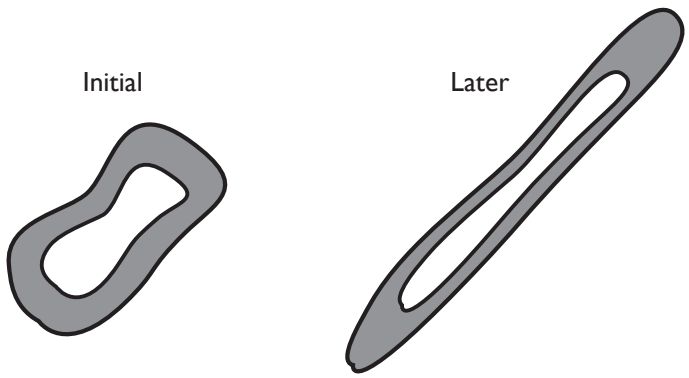

Fig. 8.5 In incompressible two-dimensional flow, a band of fluid will generally be elongated, but its area is preserved. Since vorticity is tied to fluid parcels, the values of the vorticity in the shaded area (and in the hole in the middle) are maintained; thus, vorticity gradients will increase and the enstrophy is thereby, on average, moved to smaller scales.

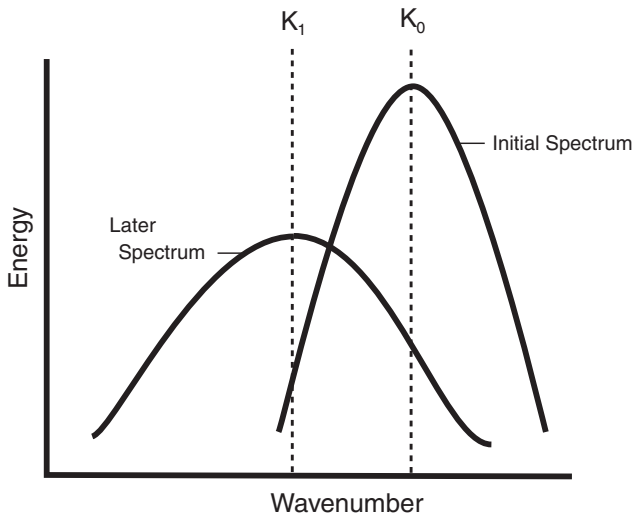

Fig. 8.6 In two-dimensional flow, the centroid of the energy spectrum will move to large scales (smaller wavenumber) provided that the width of the distribution increases — as can be expected in a nonlinear, eddying flow.

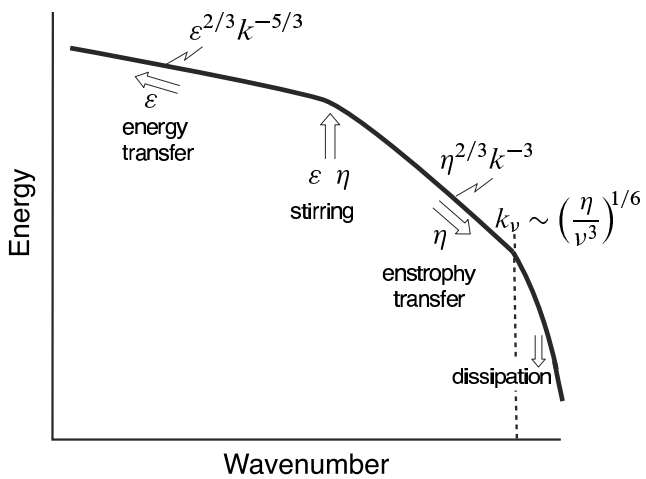

Fig. 8.7 The energy spectrum of two-dimensional turbulence. (Compare with Fig. 8.3.) Energy supplied at some rate ε is transferred to large scales, whereas enstrophy supplied at some rate η is transferred to small scales, where it may be dissipated by viscosity. If the forcing is localized at a scale k_f^{-1} then $\eta \approx k_f^2 \varepsilon$.

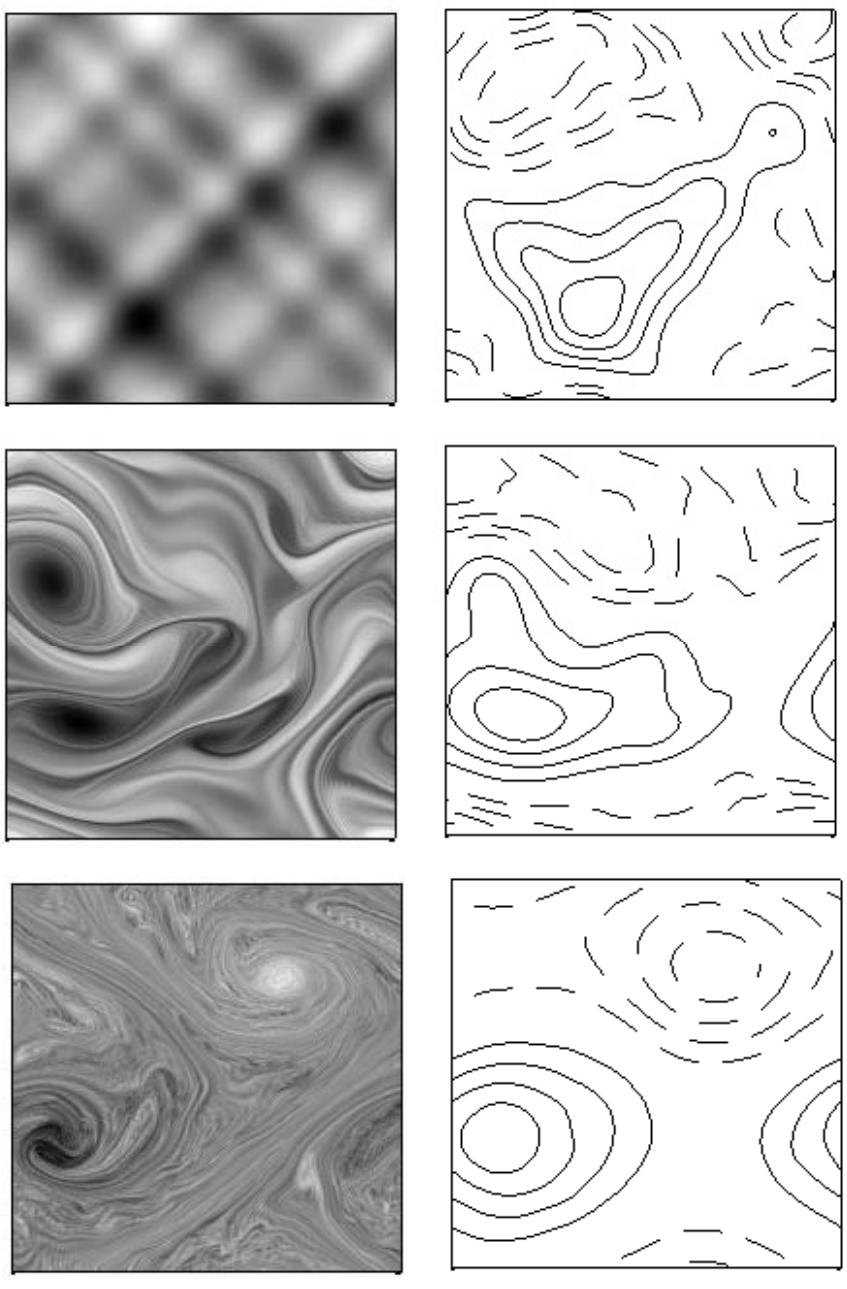

Fig. 8.8 Nearly-free evolution of vorticity (left column) and streamfunction (right column) in a doubly-periodic square domain (of length 2π) at times (from the top, and in units of inverse vorticity) $t = 0, 50$ and 260, obeying the two-dimensional vorticity equation with no forcing but with a weak viscous term. The initial conditions have just a few non-zero Fourier modes with randomly generated phases, producing a maximum value of vorticity of about three. Kelvin–Helmholtz instability leads to vortex formation and roll-up (as in Fig. 6.6), and like-signed vortices merge, ultimately leading to a state of just two oppositely-signed vortices. Between the vortices enstrophy cascades to smaller scales. The scale of the streamfunction grows larger, reflecting the transfer of energy to larger scales.

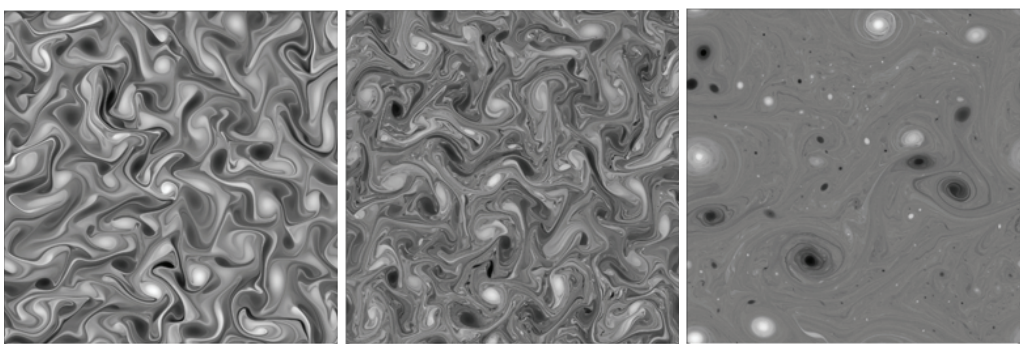

Fig. 8.9 Snapshots of the vorticity field in decaying two-dimensional turbulence, similar to Fig. 8.8, with time increasing left to right. The flow ultimately consists of a small number of vortices whose trajectories are similar to that of interacting point vortices, with occasional close encounters leading to vortex merger.

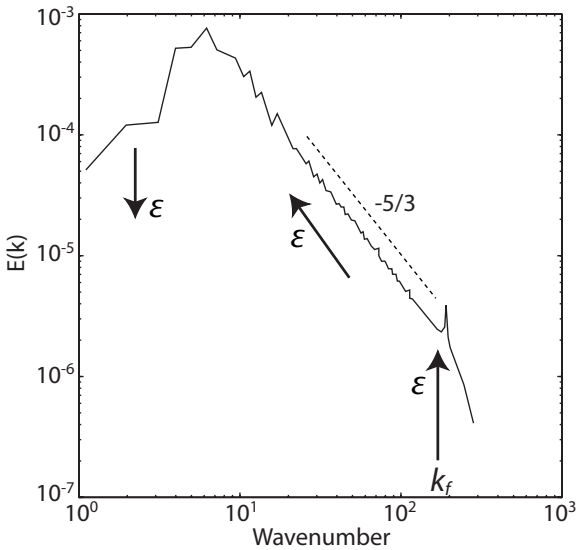

Fig. 8.10 The energy spectrum in a numerical simulation of forced-dissipative two-dimensional turbulence. The fluid is stirred at wavenumber k_f and dissipated at large scales with a linear drag, and there is an $k^{-5/3}$ spectrum at intermediate scales. The arrows indicate the direction of the energy flux, ε.[2]

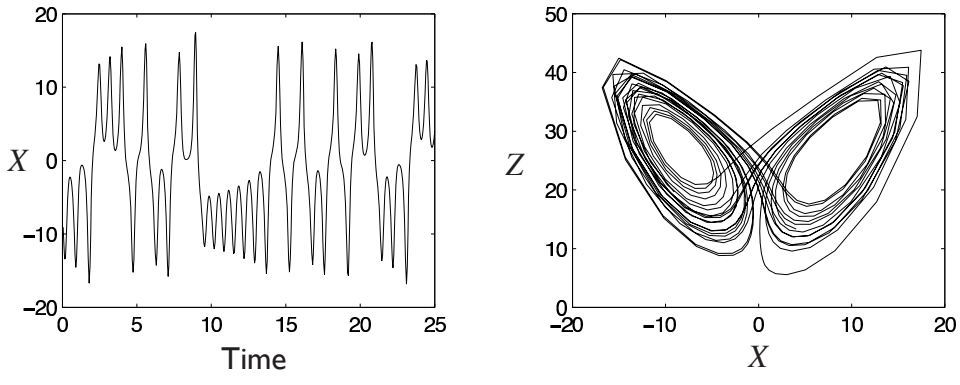

Fig. 8.11 A solution of the Lorenz equations, with $\sigma = 10$, $r = 28$ and $b = 8/3$. The left panel plots X as a function of time. The right panel plots X against Z.

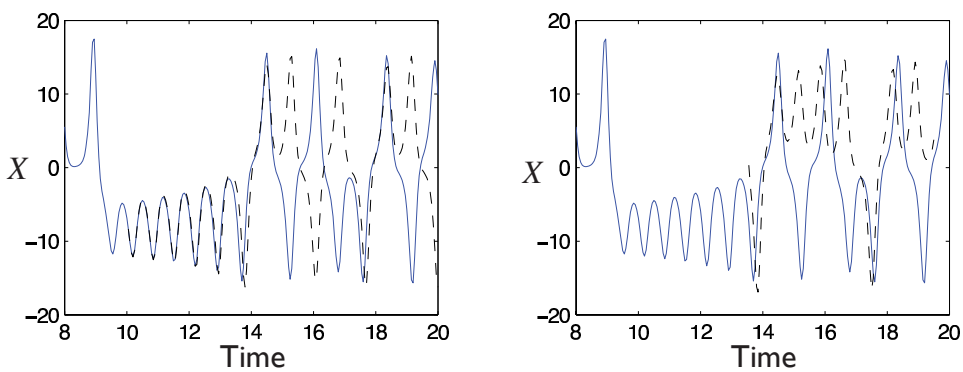

Fig. 8.12 Examples of the evolution of the Lorenz model subject to a small perturbation at time 10 (left panel) and time 13.5 (right panel). The original and perturbed systems are the solid and dashed lines, respectively.

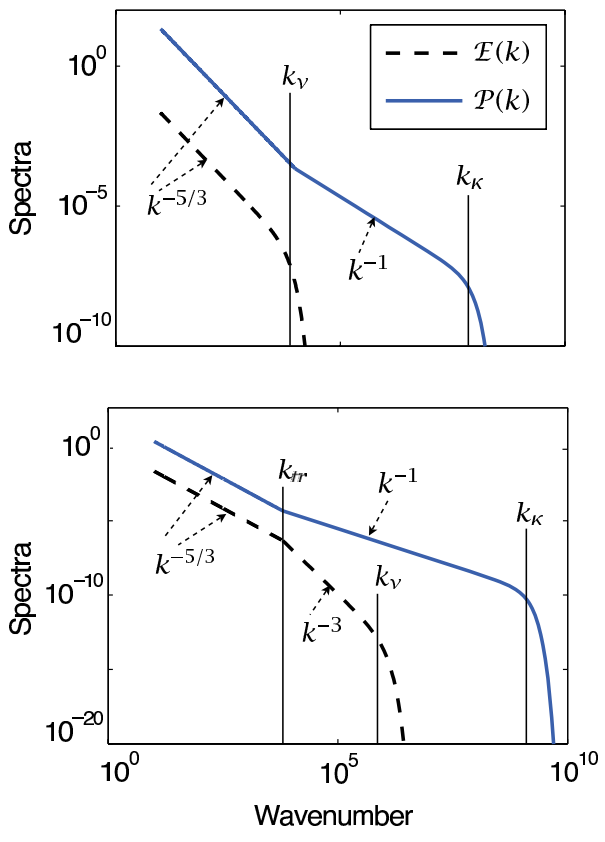

Fig. 8.13 The energy spectra, $\mathcal{E}(k)$ and passive tracer spectra $\mathcal{P}(k)$ in large Prandtl number three-dimensional (top) and two-dimensional (bottom) turbulence. In three dimensions $\mathcal{P}(k)$ is given by (8.97) for $k < k_\nu$ and by (8.106) for $k > k_\nu$. In two dimensions, if k_{tr} marks the transition between a $k^{-5/3}$ inverse energy cascade and a k^{-1} forward enstrophy cascade, then $\mathcal{P}(k)$ is given by (8.98) for $k < k_{tr}$ and by (8.107) for $k > k_{tr}$. In both two and three dimensions the tracer spectra falls off rapidly for $k > k_\kappa$.

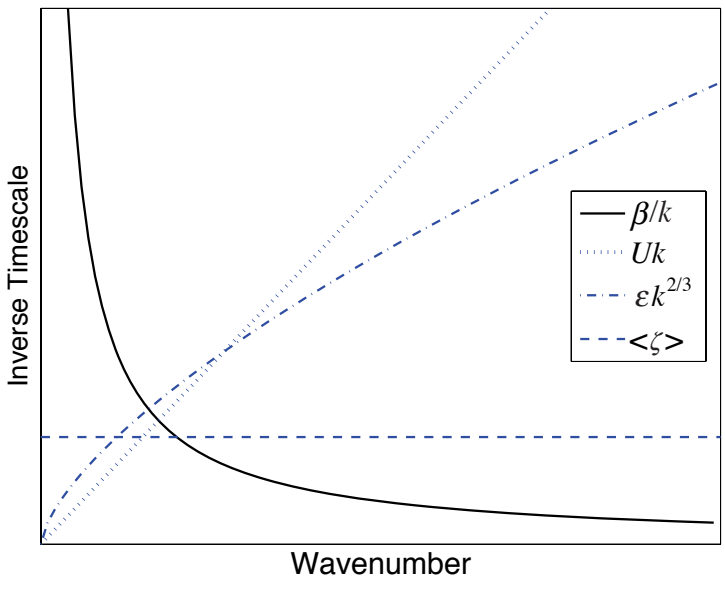

Fig. 9.1 Three estimates of the wave–turbulence cross-over, in wavenumber space. The solid curve is the frequency of Rossby waves, proportional to β/k. The other three curves are various estimates of the inverse turbulence time scale, or 'turbulence frequency'. These are the turbulent eddy transfer rate, proportional to $\varepsilon k^{2/3}$ in a $k^{-5/3}$ spectrum; the simple estimate Uk where U is an root-mean-squared velocity; and the mean vorticity, which is constant. Where the Rossby wave frequency is larger (smaller) than the turbulent frequency, i.e., at large (small) scales, Rossby waves (turbulence) dominate the dynamics.

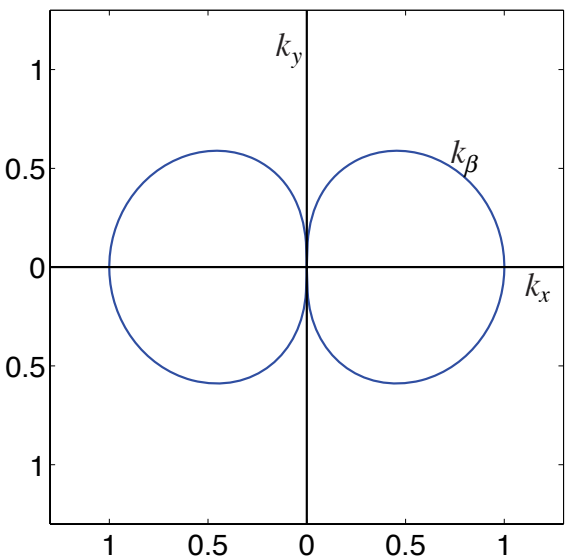

Fig. 9.2 The anisotropic wave–turbulence boundary k_β, in wave-vector space calculated by equating the turbulent eddy transfer rate, proportional to $k^{2/3}$ in a $k^{-5/3}$ spectrum, to the Rossby wave frequency $\beta k^x/k^2$, as in (9.14). Within the dumbbell Rossby waves dominate and energy transfer is inhibited. The inverse cascade plus Rossby waves thus leads to a generation of zonal flow.

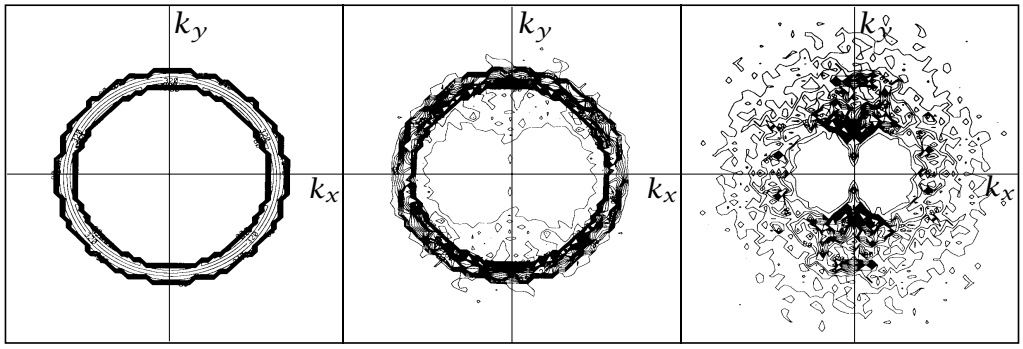

Fig. 9.3 Evolution of the energy spectrum in a freely evolving two-dimensional simulation on the β-plane. The panels show contours of energy in wavenumber (k_x, k_y) space at successive times. The initial spectrum is isotropic. The energy 'implodes', but its passage to large scales is impeded by the β-effect, and second and third panels show the spectrum at later times, illustrating the dumbbell predicted by (9.14) and Fig. 9.2.[1]

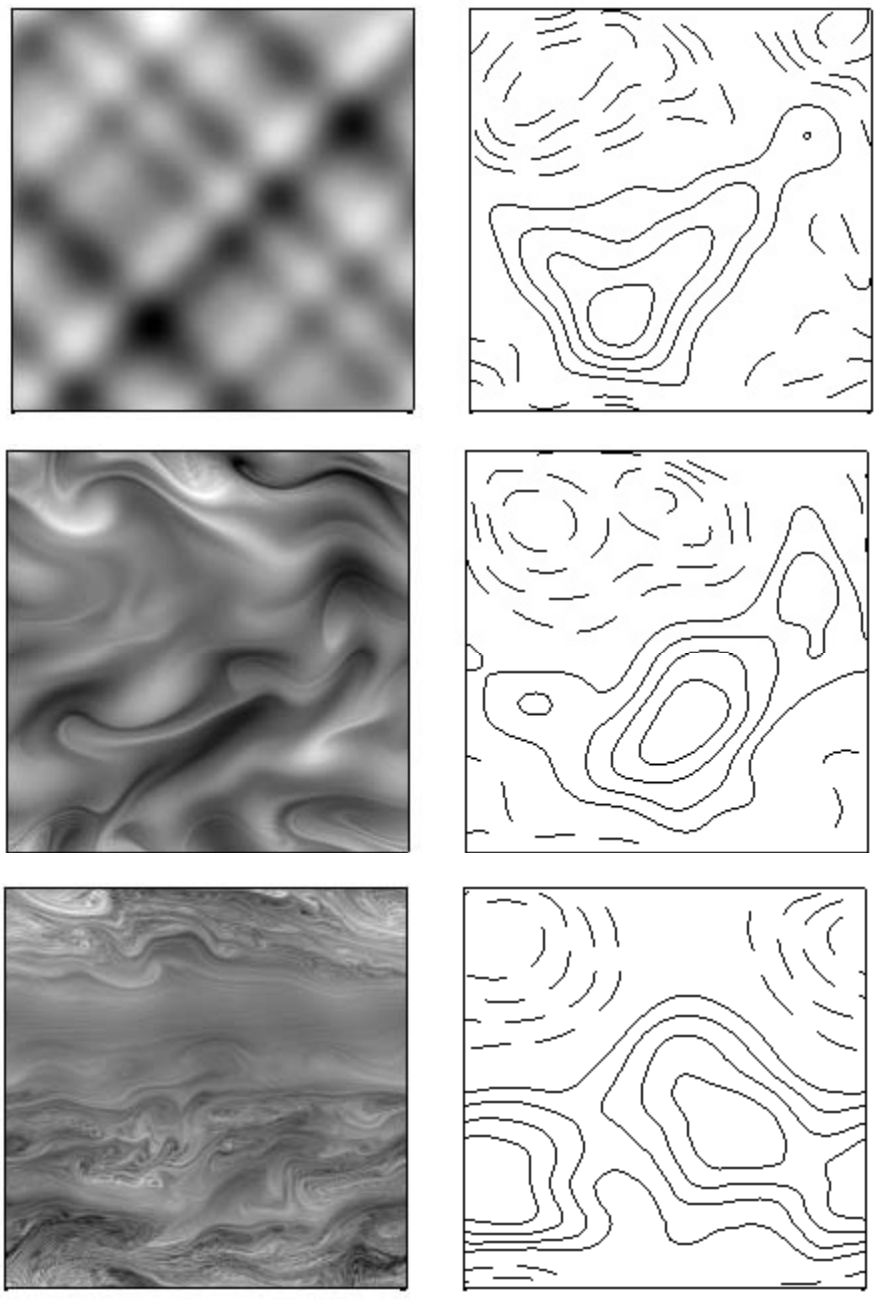

Fig. 9.4 Evolution of vorticity (greyscale, left column) and streamfunction (contour plots, right column) in a doubly periodic square domain (of length 2π) at times $t = 0, 50$ and 260 (in units of inverse vorticity), obeying (9.4) with the addition of a weak viscous term on the right-hand side. The initial conditions are the same as for Fig. 8.8, with a maximum value of vorticity of about 3. As $\beta = 3$, the β-Rossby number, $|\zeta|/\beta L$ is about unity. Compared to Fig. 8.8, vortex formation is inhibited and there is a tendency toward zonal flow.

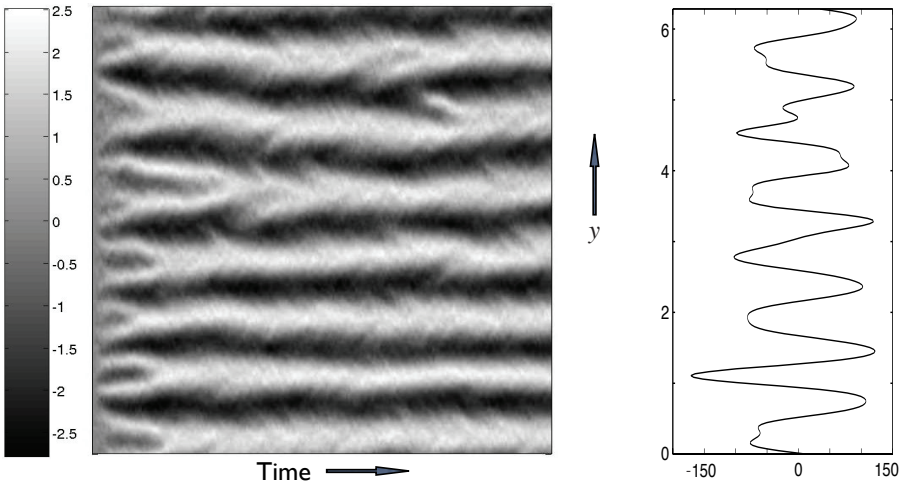

Fig. 9.5 Left: Grey-scale image of zonally averaged zonal velocity ($\overline{u}$) as a function of time and latitude (Y), produced in a simulation forced around wavenumber 80 and with $k_\beta = \sqrt{\beta/U} \approx 10$ (in a square domain of side 2π). Right: Values of $\partial^2\overline{u}/\partial y^2$ as a function of latitude, late in the integration. Jets form very quickly from the random initial conditions, and are subsequently quite steady.[2]

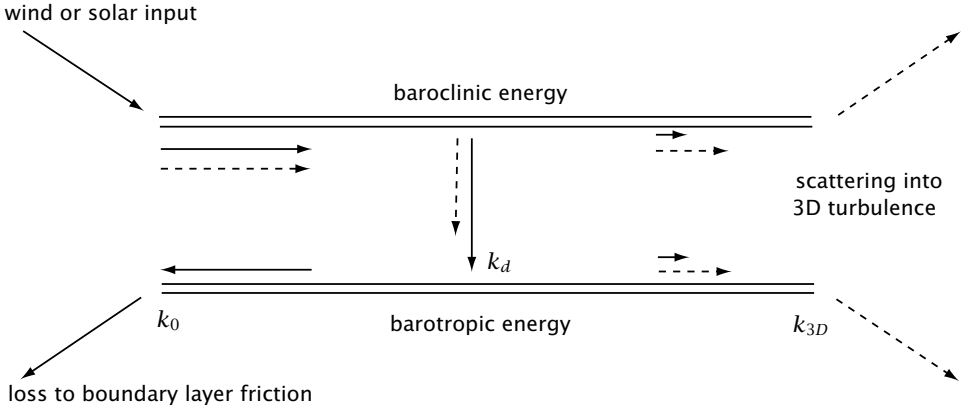

Fig. 9.6 Schema of idealized two-layer baroclinic turbulence.[3] The horizontal axis represents horizontal wavenumber, and the vertical variation is decomposed into two vertical modes — the barotropic and first baroclinic. Energy transfer is shown by solid arrows and enstrophy transfer by dashed arrows. Large-scale forcing maintains the available potential energy, and so provides energy to the baroclinic mode at very large scales. Energy is transferred to smaller baroclinic scales, and then into barotropic energy at horizontal scales comparable to and larger than the deformation radius (this is baroclinic instability), and then transferred to larger barotropic scales in an upscale cascade. The entire process of baroclinic instability and energy transfer may be thought of as a generalized inverse cascade in which the energy passes to smaller pseudowavenumber $k'^2 \equiv k^2 + k_d^2$.

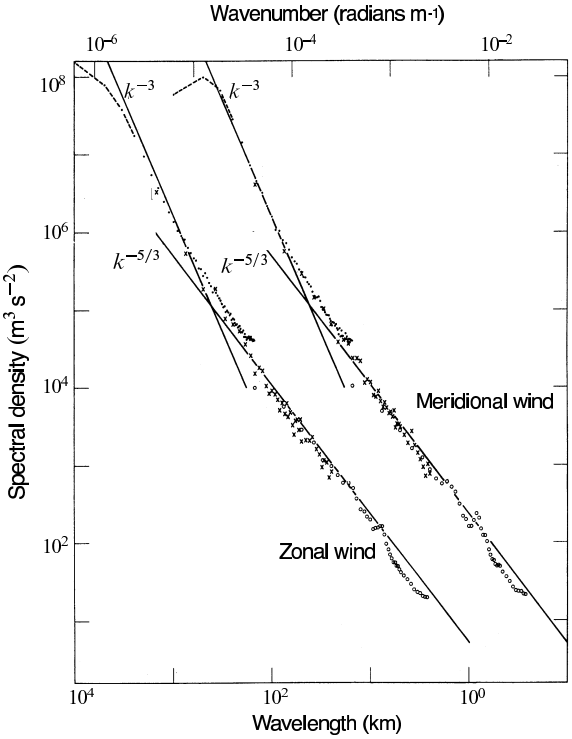

Fig. 9.7 Energy spectra of the zonal and meridional wind near the tropopause, from thousands of commercial aircraft measurements between 1975 and 1979. The meridional spectrum is shifted one decade to the right. The -3 spectrum may well be associated with a forward enstrophy cascade, but the origin of the $-5/3$ spectrum at smaller scales is not defnitively known.[4]

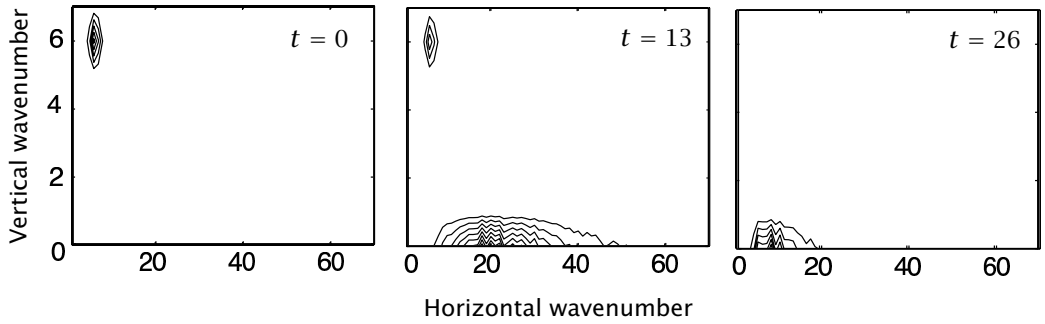

Fig. 9.8 A numerical simulation of a very idealized baroclinic lifecyle, showing contours of energy in spectral space at successive times. Initially, there is baroclinic energy at low horizontal wavenumber, as in a large-scale shear. Baroclinic instability transfers this energy to barotropic flow at the scale of the deformation radius, and this is followed by a barotropic inverse cascade to large scales. Most of the transfer to the barotropic mode in fact occurs quite quickly, between times 11 and 14, but the ensuing barotropic inverse cascade is slower. The entire process may be thought of as a generalized inverse cascade. The stratification (N^2) is uniform, and the first deformation radius is at about wavenumber 15. Times are in units of the eddy turnover time.[5]

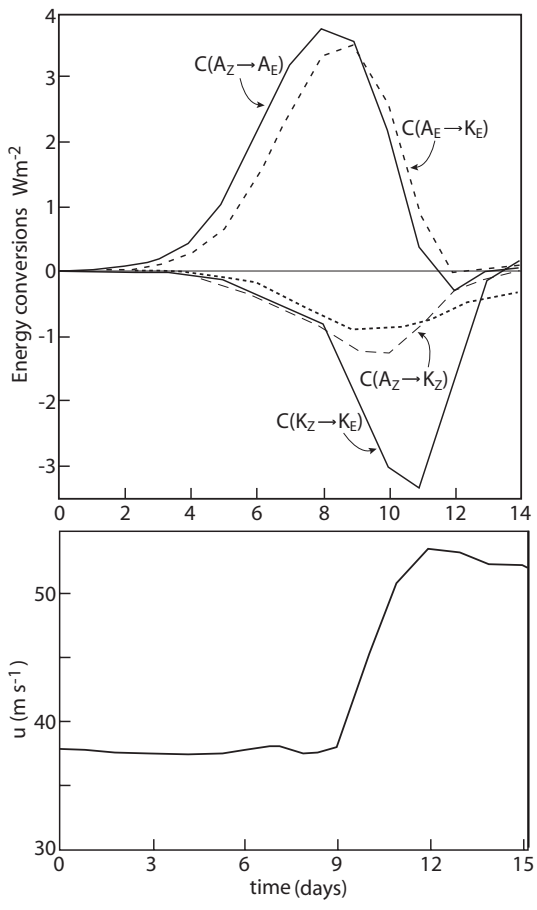

Fig. 9.9 Top: energy conversion and dissipation processes in a numerical simulation of an idealized atmospheric baroclinic lifecycle, simulated with a GCM. Bottom: evolution of the maximum zonal-mean velocity. A_Z and A_E are zonal and eddy available potential energies, and K_Z and K_E are the corresponding kinetic energies. Initially baroclinic processes dominate, with conversions from zonal to eddy kinetic energy and then eddy kinetic to eddy available potential energy, followed by the barotropic conversion of eddy kinetic to zonal kinetic energy. The latter process is reflected in the *increase* of the maximum zonal-mean velocity at about day 10.[6]

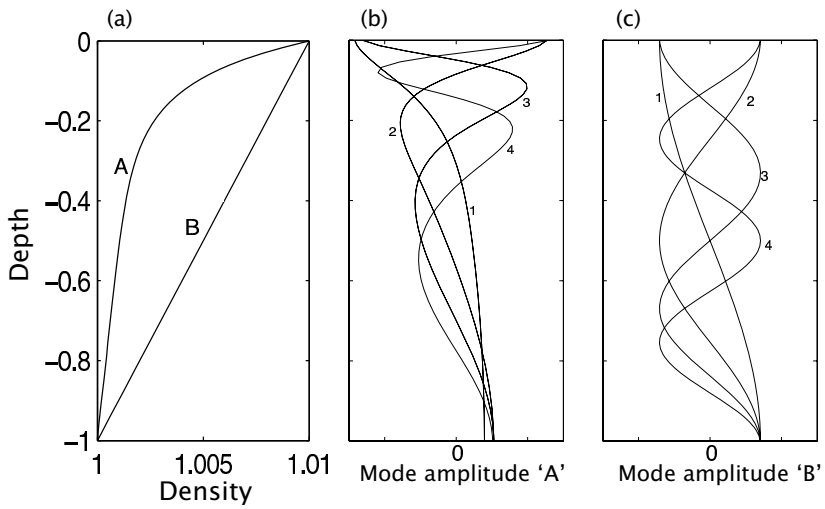

Fig. 9.10 (a) Two density profiles $[1 + (\rho_0 - \rho)/\rho_0]$, a fairly realistic oceanic case with enhanced stratification in the upper ocean (profile A), and uniform stratification (profile B). (b) and (c) The first four baroclinic modes [eigenfunctions of (9.71)]. With profile B the eigenmodes are cosines, whereas in profile A they have a larger amplitude in the upper ocean. The number of zero crossings is equal to the mode number.

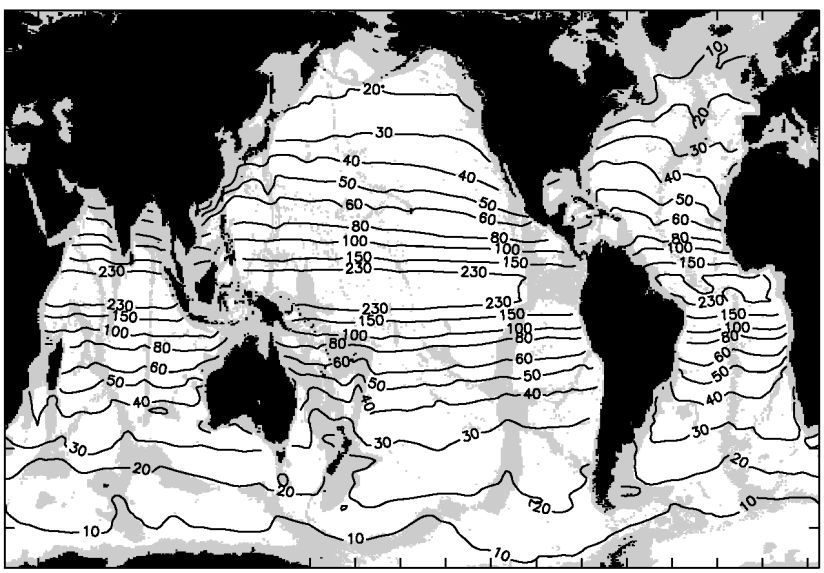

Fig. 9.11 The oceanic first deformation radius L_d, calculated using the observed stratification and an equation similar to (9.71). Near equatorial regions are excluded, and regions of ocean shallower than 3500 m are shaded. Variations in Coriolis parameter are responsible for much of large-scale variability, although weak stratification also reduces the deformation radius at high latitudes.[7]

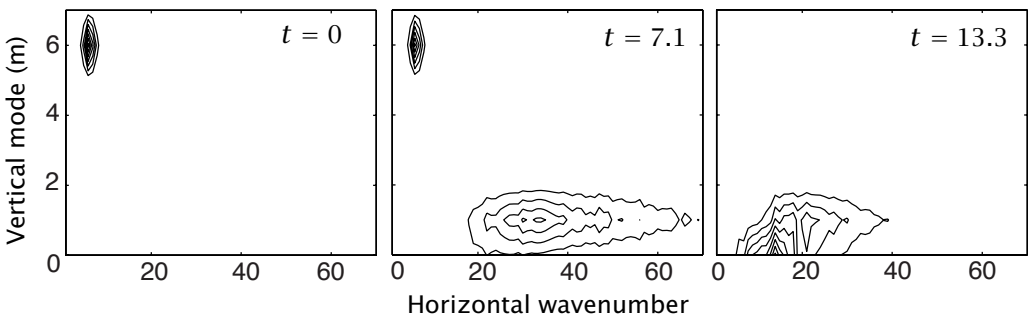

Fig. 9.12 Idealized baroclinic lifecyle, similar to that in Fig. 9.8, but with enhanced stratification of the basic state in the upper domain, representing the oceanic thermocline.

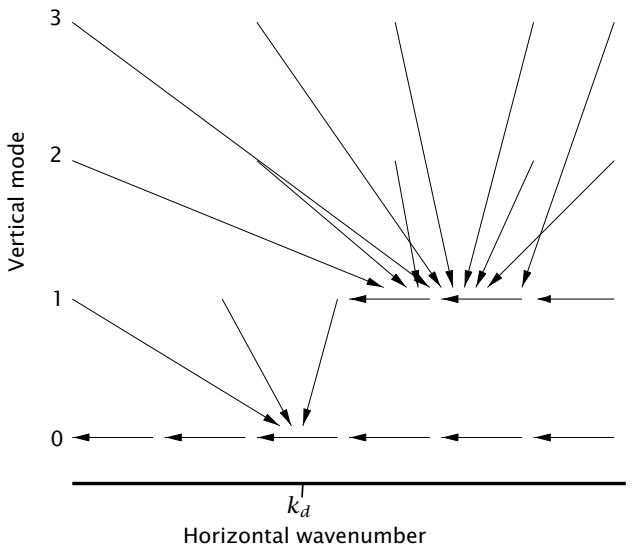

Fig. 9.13 Energy transfer paths as a function of vertical mode and horizontal wavenumber, in a fluid with an oceanic stratification; i.e., with a thermocline. Vertical mode 0 is the barotropic mode.

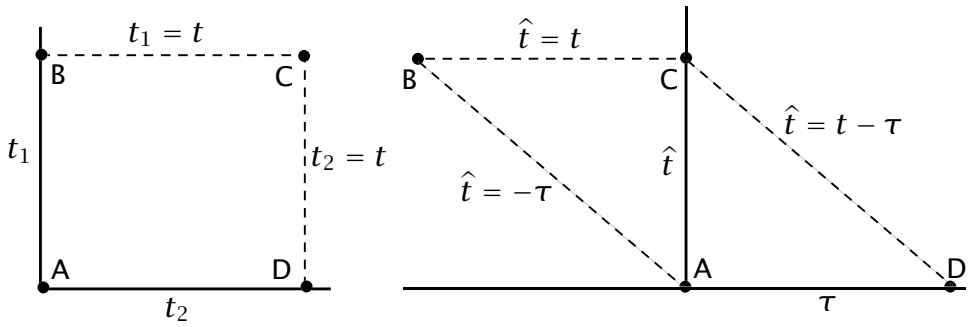

Fig. 10.1 Changes of time variables involved in (10.16) and (10.32). The original two-dimensional integral is over the rectangle ABCD. Defining $\tau = t_2 - t_1$ and $\hat{t} = t_1$, then the area is spanned by $[\hat{t} = (0, t),\ \tau = (t - \hat{t}, -\hat{t})]$ as in (10.16), or by $[\tau = (0, t),\ \hat{t} = (0, t - \tau)]$ (i.e., ACD) plus $[\tau = (-t, 0),\ \hat{t} = (-\tau, t)]$ (i.e., ABC) in (10.32).

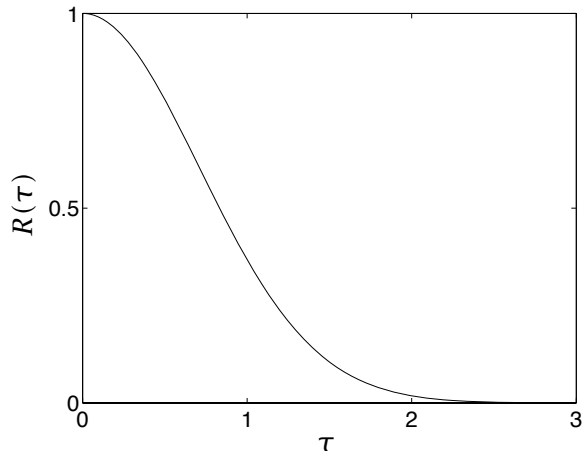

Fig. 10.2 Schematic of a velocity correlation function in turbulent flow with correlation time $\tau_{corr} = \mathcal{O}(1)$. For small times, $\tau \ll \tau_{corr}$, $R(\tau) \approx 1$. For large times, $\tau \gg \tau_{corr}$, $R(\tau) \ll 1$. We may define the correlation time by $\tau_{corr} = \int_0^\infty R(\tau)\,\mathrm{d}\tau$.

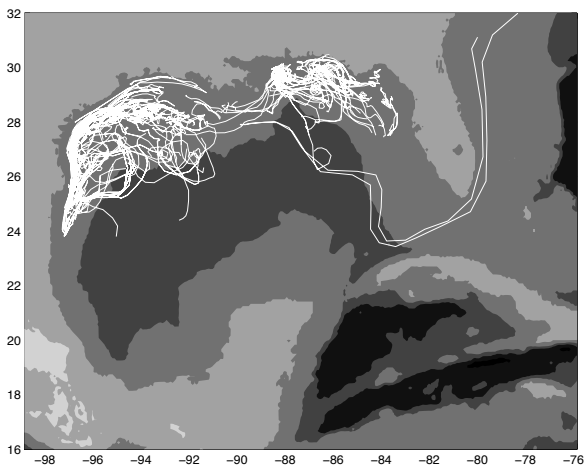

Fig. 10.3 Trajectories of surface drifters in the Gulf of Mexico, each truncated to produce paths of just 25 days. The drifters were released as part of 'SCULP' — the Surface CUrrent and Lagrangian drift Program.[1]

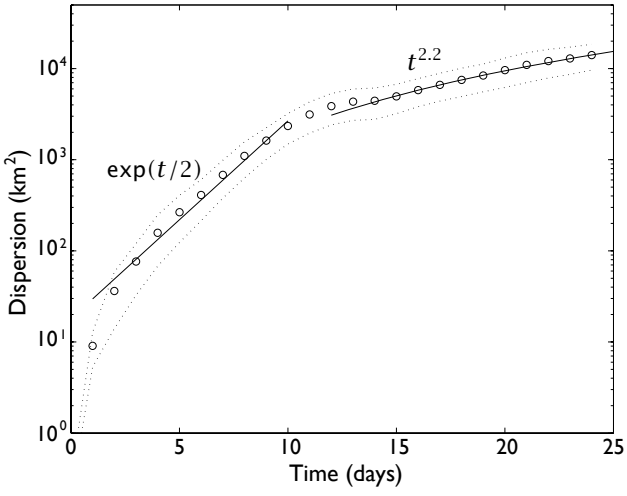

Fig. 10.4 Relative dispersion (the mean-square separation) for 140 drifter pairs as a function of time. The analysis utilizes all drifter pairs which come within 1 km of each other during their lifetimes.

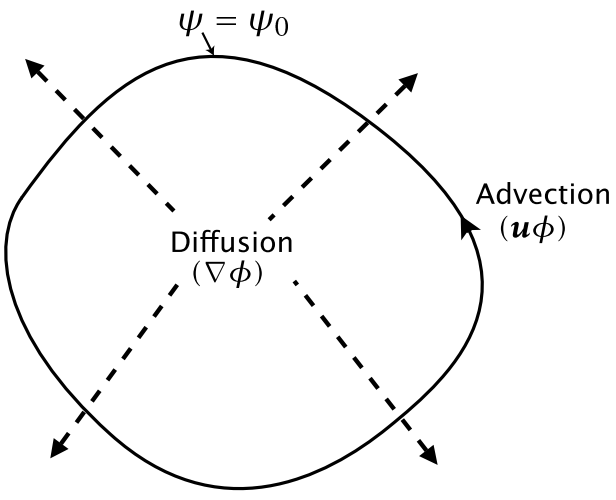

Fig. 10.5 If an extremum of a tracer ϕ exists in the fluid interior, then diffusion will provide a downgradient tracer flux. Over an area bounded by a streamline, or by an isoline of ϕ, the net advective flux is zero. Thus, the diffusion cannot be balanced by advection, and in a steady state no extrema can exist.

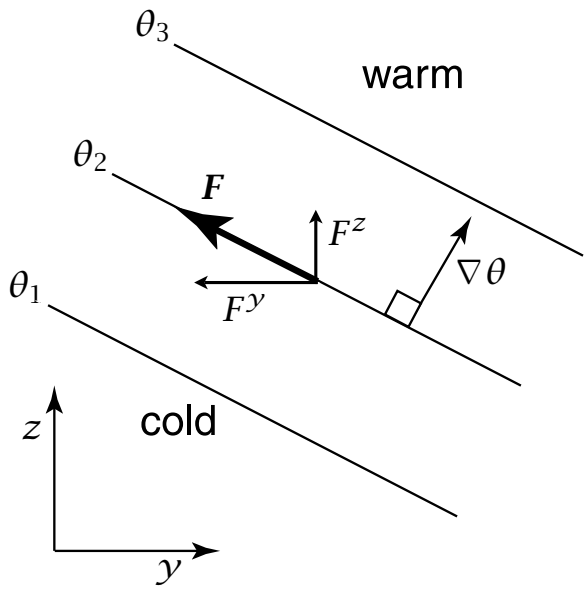

Fig. 10.6 The GM skew fluxes arising from sloping isotherms. The flux itself, $\boldsymbol{F}$, is parallel to the isotherms, with the horizontal flux being directed down the horizontal gradient but the vertical flux being upgradient. The effect of the vertical flux is to lower the centre of gravity of the fluid, and reduce the potential energy. The horizontal flux tries to make the temperature more uniform in the horizontal direction. The net effect of the skew flux is to *flatten* the isotherms.

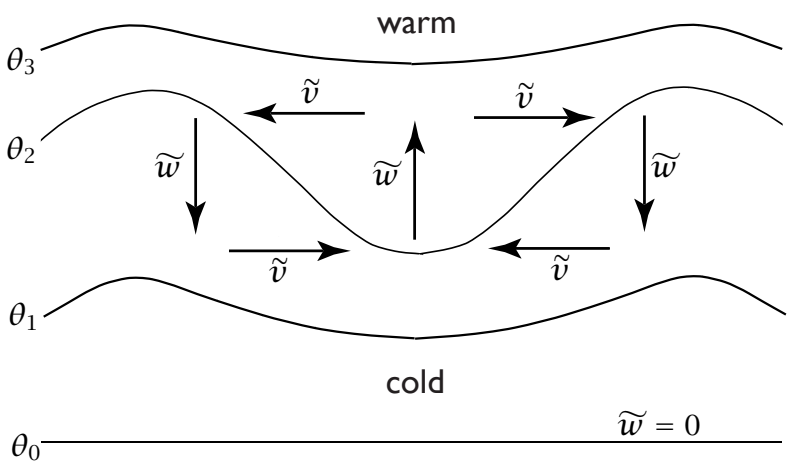

Fig. 10.7 The eddy-induced velocities in the Gent–McWilliams parametrization. The induced circulation attempts to flatten the sloping isopycnals. The induced vertical velocity, $\widetilde{w}$, is zero on flat isopycnals.